High-performance hybrid supercapacitor of mixed-valence manganese oxide/N-doped graphene aerogel nanoflower using an ionic liquid with a redox additive as the electrolyte: *In situ* electrochemical X-ray absorption spectroscopy

Nattapol Ma [a], Nutthaphon Phattharasupakun [a], Juthaporn Wutthiprom [a], Chan Tanggarnjanavalukul [a], Phatsawit Wuanprakhon [a], Pinit Kidkhunthod [b], Montree Sawangphruk [a, *]

[a] *Department of Chemical and Biomolecular Engineering, School of Energy Science and Engineering, Vidyasirimedhi Institute of Science and Technology, Rayong 21210, Thailand*
[b] *Synchrotron Light Research Institute (Public Organization), Nakhon Ratchasima 30000, Thailand*

ARTICLE INFO

ABSTRACT

Although electrochemical double layer capacitors (EDLCs) have high specific power, their specific energy is rather low. To address this issue, a composite material between EDLC-type N-doped graphene aerogel (N-rGO$_{ae}$) with an N-doped content of ca. 8 at% and pseudocapacitor-type mixed-valence manganese oxide (MnO$_x$) nanoparticles with a diameter of <20 nm was synthesized and used as the electrode material of hybrid supercapacitors. In addition, a new electrolyte of ionic liquid electrolyte 1-butyl-1-methylpyrrolidinium dicyanamide ([BMP][DCA]) with a redox additive (K$_4$[Fe(CN)$_6$]) was employed to further improve the performance of the hybrid supercapacitor. The as-fabricated supercapacitor exhibits an excellent specific energy and power of 44.7 Wh kg^{-1} and 4551.4 W kg^{-1}, respectively. *In situ* electrochemical X-ray absorption spectroscopy (XAS) was also used to investigate the charge storage mechanism of the mixed-valence MnO$_x$ in the composite. Interestingly, with the presence of redox additive in the electrolytes, a wide oxidation state variation range of Mn in the MnO$_x$/N-rGO$_{ae}$ composite can be observed indicating high redox activities and confirming the faradaic charge transfer interaction between redox additive and MnO$_x$. Furthermore, the *in situ* XAS result also confirms the reversibility of the redox reaction of MnO$_x$ showing that the hybrid supercapacitor using the ionic liquid electrolyte with a redox additive in this work may be practically used in high-energy applications.

© 2018 Elsevier Ltd. All rights reserved.

1. Introduction

Supercapacitors (SCs) are energy-storage devices mainly used in high-power applications such as accelerative and regenerative systems in electric vehicles (EVs) and high penetration of the wind/solar generation in grid-storage system [1–3] due to their high specific power (~500–10000 W kg^{-1}) and long cycling stability (>300,000 cycles). Also, they are much safer when compared to Li-ion batteries due to their charge storage mechanisms [2,4]. The SCs rely on two charge storage mechanisms at the electrode-electrolyte interface including the reversible physisorption of electrolyte ions on the active surface of electrode materials so-called electrochemical double layer capacitive (EDLC) behavior and a fast surface redox reaction or pseudo-capacitive behavior. However, the specific energy of SCs is rather low, 5–30 Wh kg^{-1} when compared to 20–250 Wh kg^{-1} of batteries [5]. Thus, the challenge of SC research field is to improve specific energy while retaining its advantages i.e., high specific power, stability, and reliability.

Among various supercapacitor materials, manganese oxide (MnO$_2$) is a promising candidate since it can deliver a high theoretical capacitance of 1233 F g^{-1}. It stores charges via the surface redox reaction. MnO$_2$ is also nontoxic, cheap, and abundant in

* Corresponding author.
    E-mail address: montree.s@vistec.ac.th (M. Sawangphruk).

nature. However, the theoretical capacitance of MnO_2 has not yet been achieved due to its intrinsically poor electrical conductivity and poor stability [6–8]. To overcome this limitation, MnO_2 has been composited with graphene-related materials since graphene exhibits good EDLC behavior, conductivity, stability, and surface area. In addition, introducing N- and O-containing functional groups to graphene structure can increase ionic conductivity and generate active sites via the surface redox reactions [9–11]. Additionally, the surface redox kinetics could be enhanced by turning manganese oxide into a mixed-valence phase. The coexisting of Mn^{2+}, Mn^{3+}, and Mn^{4+} enables the availability of ionic defects and electronic defects, promoting the fast kinetics of surface pseudo-capacitive behavior [12].

Apart from the development of hybrid electrode materials storing charges via both EDLC and pseudocapacitance, the addition of redox mediators to the aqueous electrolytes has recently been proven as a novel strategy to improve the energy density of SCs by enabling a fast electron transfer (redox reaction) at the electrode-electrolyte interface. Redox active electrolytes can act as active ions performing both electrical double layer and reversible faradaic charge storage [13]. Recently, the hydroquinone/quinine redox additive in 1 M H_2SO_4 exhibited a remarkable enhancement on the energy density of activated carbon from 10.1 to 30.6 Wh kg^{-1} [14]. KI in H_2SO_4 was also reported with a significant improvement in the specific capacitance of activated carbon from 472 to 912 F g^{-1} [15]. In addition, $K_3[Fe(CN)_6]/K_4[Fe(CN)_6]$ redox couple in KOH and Na_2SO_4 with several electrode materials can improve the overall electrochemical performance of the SCs [13,16,17]. These improvements on the specific capacitance and energy density are comparable to that of conventional batteries, also being much simpler and safer when compared to a complex electrode preparation procedure of Li-ion batteries [13,18]. However, the study of redox active electrolytes has been focused mainly on aqueous-based electrolytes and a few reports have been done on non-aqueous electrolytes (only with pure EDLC active material) [19,20]. As known, the aqueous-based electrolytes provide rather low working voltage since water is thermodynamically decomposed at 1.23 V vs. NHE at the standard condition. Therefore, the use of non-aqueous electrolytes, especially ionic liquid has received much attention for use in SCs due to their excellent chemical and thermal stability, wide electrochemical potential window, and high safety [21,22]. In addition, the use of ionic liquid electrolyte with large potential window leads to a significant improvement of the specific energy of SCs as compared to those in the aqueous electrolyte.

Herein, we report a new strategy for enhancement in the specific energy of hybrid SCs by adding a redox additive to the ionic liquid electrolyte. Potassium ferrocyanide ($K_4[Fe(CN)_6]$) was added to 1-butyl-1-methylpyrrolidinium dicyanamide ([BMP][DCA]) and used as the electrolyte for high-performance SCs. A mixed-valence manganese oxide/N-doped reduced graphene oxide nanoflower composite (MnO_x/N-rGO$_{ae}$) was also used as a new active composite material for high-performance hybrid SCs. For the best of our knowledge, ionic liquid with redox additive has not yet been used as the electrolyte of the hybrid SCs. Also, MnO_x nanoparticles incorporated in N-rGO$_{ae}$ with a unique nanoflower morphology have not yet been used as the active material of ionic-liquid-based SCs. In addition, the charge storage mechanism of the MnO_x/N-rGO$_{ae}$ has been investigated by an *in situ* electrochemical X-ray absorption spectroscopy (XAS). Interestingly, with the presence of redox additive in the ionic liquid electrolyte, a wide oxidation state variation range of Mn in the MnO_x/N-rGO$_{ae}$ composite can be observed indicating high redox activities.

2. Experimental

2.1. Chemical and materials

Graphite (<20 μm, Sigma-Aldrich), sulfuric acid (H_2SO_4, 98%, QRec), nitric acid (HNO_3, 67%, QRec), hydrogen peroxide (H_2O_2, 30%, Chem-supply), potassium permanganate ($KMnO_4$, Carlo Erba), polyvinylidene fluoride (PVDF, Mw~534,000, Sigma-Aldrich), hydrazine hydrate (N_2H_4, 99%, Loba Chemie), sodium sulfate anhydrous (Na_2SO_4, UNIVAR), potassium ferrocyanide (QRec), 1-butyl-1-methylpyrrolidinium dicyanamide ([BMP][DCA], Sigma-Aldrich), sodium nitrate ($NaNO_3$, Ajax Finechem), ethylene glycol (99.5%, Sigma−Aldrich), manganese(II) acetate tetrahydrate ($Mn(CH_3COO)_2 \cdot 4H_2O$, 99%, Acros Organics), polyvinyl-pyrrolidone (10,000 g mol^{-1}, Sigma-Aldrich), N-Methyl-2-Pyrrolidone (NMP, 99.5%, QRec) are of analytical grade and used without further purification. Deionized water was purified by using Milli-Q system (DI water, 15 MΩ cm, Millipore). Carbon fiber paper (CFP, SGL CARBON SE in Germany) was used as a substrate.

2.2. Syntheses of manganese oxide nanoparticles and manganese oxide/N-doped reduced graphene oxide nanoflower composite

Firstly, 1000 ml of ethylene glycol was heated at 160 °C for 10 min to remove water and then cooled down to 80 °C. Next, 10 g of polyvinyl-pyrrolidone (10,000 g mol^{-1}) and 5 g of $Mn(CH_3COO)_2 \cdot 4H_2O$ were subsequently added to ethylene glycol while stirring. After 30 min, the reddish product suspension was obtained and cooled down to room temperature [23,24].

The synthesis procedure of mixed-valence manganese oxide/N-doped reduced graphene oxide nanoflower composite (MnO_x/N-rGO$_{ae}$) was modified from an aerogel synthesis method [25] as follows; GO (150 mg) produced by a modified Hummer's method [24,26] was dispersed in the as-prepared manganese oxide suspended in ethylene glycol (75 ml) by ultrasonication for 2 h. Then, 0.5 M hydrazine hydrate was added to the suspension and consequently transferred to the Teflon-lined stainless-steel autoclave. The solvothermal process was conducted at 80 °C in an oven (SLN, POL-EKO APARATURA) for 72 h. The hydrogel product was soaked in Milli-Q water for 2 days to get rid of the hydrazine residual from the hydrogel. The hydrogel was eventually frozen via liquid nitrogen before being placed in a freezing dryer machine (Labconco, 2.5 L benchtop freeze-dry systems) at −50 °C for 2 days.

2.3. Preparation of ionic liquid electrolyte with redox mediator

To prepare the hybrid electrolyte, 1 mM $K_4[Fe(CN)_6]$ was added to 5 ml [BMP][DCA] and stirred for 24 h. Note, [BMP][DCA] ionic liquid has a strong coordinating property leading to a good capability to dissolve the metal salts [27−29].

2.4. Morphological and structural characterizations

Field-Emission Scanning Electron Microscopy (FE-SEM, JSM-7001F, JEOL Ltd.), Energy Dispersive X-ray Spectroscopy (EDX, Oxford instruments), and Transmission electron microscopy (TEM, JEOL Ltd., Japan) were employed to characterize the morphologies and surface compositions of the as-synthesized samples. The structural properties and surface compositions were further investigated utilizing Raman spectra (Senterra Dispersive Raman Microscope, Bruker) and X-ray photoelectron spectroscopy (XPS, JPS-9010MC, JEOL Ltd., with MgKα), respectively. X-ray powder diffraction (XRD) patterns were obtained using D8 ADVANCE with

DAVINCI design (Bruker, CuKα of 1.5418 Å). In situ Mn K-edge fluorescent X-ray absorption spectroscopy (XAS) was characterized at Synchrotron Light Research Institute BL. 5.2 (Public Organization), Thailand. Note, XAS was equipped with Ge (220) double-crystal monochromator with an energy range of 3440−12100 eV.

2.5. Fabrication of the supercapacitors and electrochemical evaluation

Electrodes were prepared by mixing MnO_x/N-GO$_{ae}$, carbon black (conductive material), and PVDF (binder) in a weight ratio of 8:1:1, respectively and dissolved in NMP. The mixture was homogenously dispersed via ultrasonication for 24 h. Then the obtained slurry was spray-coated on carbon fiber paper (a diameter of 1.58 cm) [30] with an active material mass loading of 3−4 mg per cell utilizing an 0.3-mm nozzle airbrush (Paasche Airbrush Company, USA) and dried in a vacuum oven at 60 °C for 24 h. Hydrolysed polyethylene film with a thickness of 25 μm and glass microfiber (Whatman) were utilized as the separator of supercapacitors for aqueous-based and ionic liquid-based cell, respectively. 0.5 M Na_2SO_4(aq), 0.5 M Na_2SO_4(aq) with 1 mM K_4[Fe(CN)$_6$], [BMP][DCA], and [BMP][DCA] with 1 mM K_4[Fe(CN)$_6$] were used as electrolytes. The coin cell was then assembled by pressing with a crimper machine at 2000 psi (CR2016). The electrochemical performances were evaluated by cyclic voltammetry (CV), galvanostatic charge/discharge (GCD), and electrochemical impedance spectroscopy (EIS) technique using Metrohm AUTOLAB potentiostat (PGSTAT302N). Note, the stability test was performed using the GCD technique at 2 A g^{-1} with 75% working potential.

2.6. In situ electrochemical X-ray absorption spectroscopy

In situ XAS measurement was performed to examine the oxidation state of Mn under certain applied potential via chronoamperometry technique. In this measurement, a 3-electrode set up using the as-prepared MnO_x/N-GO$_{ae}$ on CFP as a working electrode, platinum wire as a counter electrode, SCE as a reference electrode for the aqueous-based electrolyte, and Ag/Ag$^+$ for the ionic-liquid based electrolyte was carried out in 0.5 M Na_2SO_4(aq), 0.5 M Na_2SO_4(aq) with 1 mM K_4[Fe(CN)$_6$], [BMP][DCA], and [BMP][DCA] with 1 mM K_4[Fe(CN)$_6$] electrolyte. Note, the test cell with the dimension of 2 cm × 2 cm × 3.5 cm was fabricated from acrylic sheets with a square opening space on one of the 2-cm^2 sides (covered by a Kapton tape). Reference and counter electrodes were located alongside with the working electrode at ca. 1 cm (out of X-rays range). *In situ* measurement was performed at steady-state
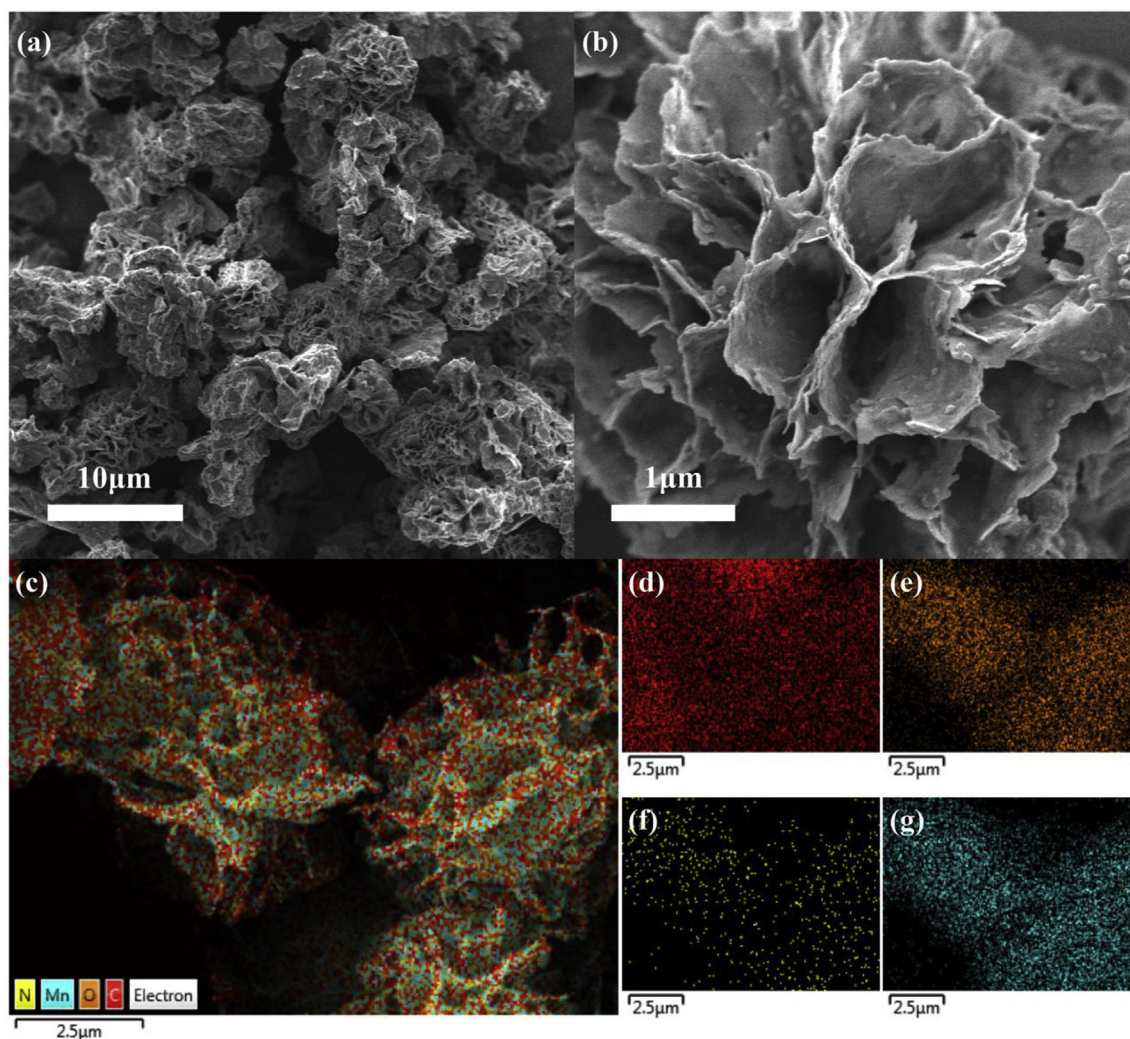

Fig. 1. FE-SEM at (a) low magnification and (b) high magnification as well as EDX mapping of MnO_x/N-GO$_{ae}$ showing (e) all elements, (f) carbon, (g) oxygen, (h) nitrogen, and (i) manganese of mixed-valence manganese oxide/N-doped reduced graphene oxide nanoflower (MnO_x/N-rGO$_{ae}$).
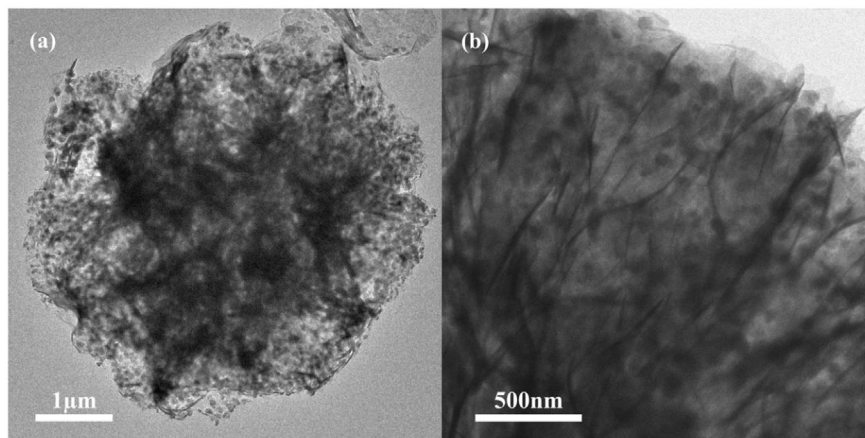
Fig. 2. TEM images at (a) low magnification and (b) high magnification of the MnO_x/N-rGO_{ae}.

current by retaining the working electrode at a specific potential of interest for at least 15 min before the characterization [30–32].

3. Results & discussion

3.1. Morphological and structural properties

The MnO_x/N-rGO_{ae} was synthesized via a one-step solvothermal synthesis then dehydrated by freezing-dry method to obtain a brown aerogel powder. Low magnification (Fig. 1a) and high magnification (Fig. 1b) field-emission scanning electron microscopy (FESEM) images of the MnO_x/N-rGO_{ae} demonstrate a uniform rearrangement of rGO sheets with a unique 3D nanoflower-like

framework decorated with MnO_x nanoparticles. The unique 3D graphene framework can enhance the electronic conductivity, electrolyte transportation, and provide active surfaces for storing charges [30]. The EDX mapping of MnO_x/N-rGO_{ae} (Fig. 1c–g) shows four main elements of C, Mn, O, and N confirming the composite material of MnO_x/N-rGO_{ae} with a homogenous dispersion of Mn nanoparticles on carbon framework. The corresponding 3D structure of MnO_x/N-rGO_{ae} is also illustrated by TEM images (Fig. 2a and b) for which the dark spots represent MnO_x nanoparticles decorated on a thin layer of graphene and surrounded by vertically aligned graphene sheets (dark stripes). In addition, the incorporated MnO_x clusters with a small diameter can provide higher active site as compared to a larger cluster [24]. Note, a TEM image of
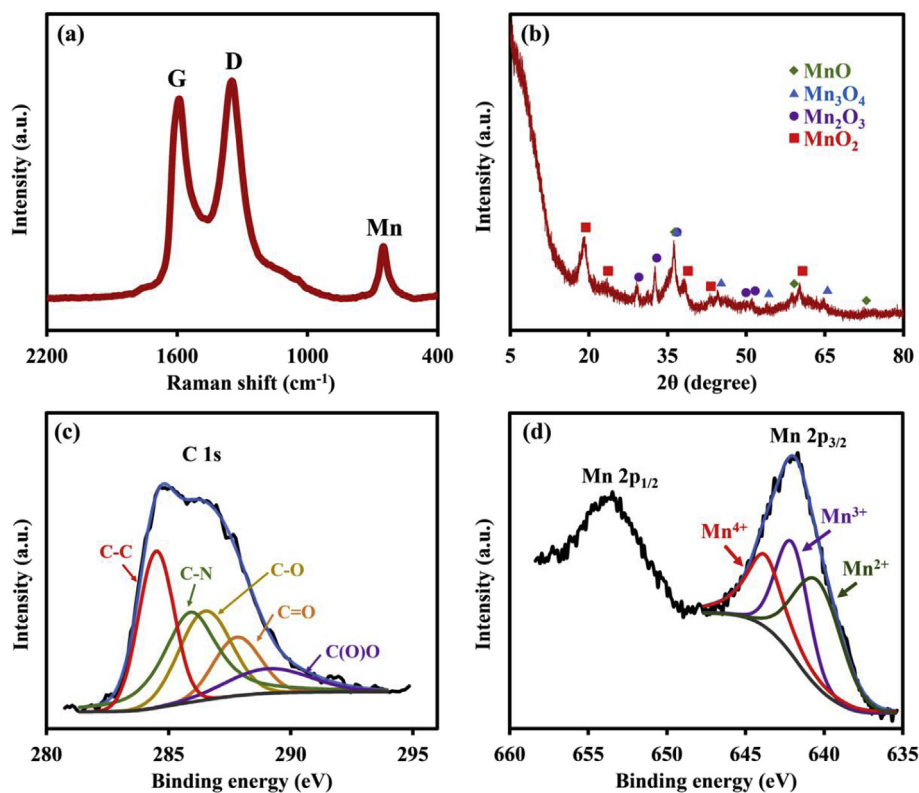

Fig. 3. (a) Raman and (b) XRD pattern as well as (XPS spectra of (c) C 1s and (d) Mn 2p of the MnO_x/N-rGO_{ae}.

the as-synthesized MnO_x nanoparticles is shown in Fig. S1.

Further characterization of the MnO_x/N-rGO$_{ae}$ were also investigated using Raman, XRD, and XPS techniques. The Raman spectrum of MnO_x/N-rGO$_{ae}$ (Fig. 3a) exhibits the combination of both rGO and MnO_x characteristic peaks. Two notable peaks of rGO at 1590.5 cm^{-1} and 1348 cm^{-1} can be attributed to the G-band (sp^2-hybridized, C–C bond) and D-band (defects/disordered) vibration modes of rGO, respectively. An intensity ratio of D to G band (I$_D$:I$_G$) is 1.09. A high intensity of defective characteristic (D-band) originates from the presence of oxygen from GO and nitrogen from N-doped functional groups [33]. A distinct peak at 650.5 cm^{-1} indicates the perpendicular vibration of Mn–O to the direction of octahedral double chains of manganese oxide [33,34]. The XRD result (Fig. 3b) shows the mixed-valence manganese oxide crystalline structures including MnO_2, Mn_2O_3, Mn_3O_4, and MnO formed after the reduction reaction by ethylene glycol and hydrazine hydrate under the solvothermal condition [35]. Note, the semi-quantitative (S-Q) weight percentages of MnO_2, Mn_2O_3, Mn_3O_4, and MnO are 24.2%, 29.0%, 33.9%, and 12.9%, respectively. In addition, the valence state of the as-synthesized MnO_x/N-rGO$_{ae}$ was investigated by XPS technique. A wide-scan XPS spectrum of MnO_x/N-rGO$_{ae}$ in Fig. S2 confirms all elements in the sample including 35.59 at% Mn, 31.67 at% C, 24.8 at% O, and 7.94 at% N. Further information can be obtained from the narrow-scan XPS spectra of C 1s (Fig. 3c) and Mn 2p (Fig. 3d). The C 1s XPS shows five notable peaks corresponding to non-oxygenated carbon (284.5 eV), C–N bond (286.5 eV), carbonyl group (287.8 eV), and carboxylate group (289.1 eV) with an additional C–N bond at 285.9eV [36]. For the Mn 2p XPS, it composes of Mn 2p$_{1/2}$ peak at 653.6 eV and Mn 2p$_{3/2}$ peak at 642.1 eV. Mn 2p$_{3/2}$ peak can be deconvoluted into three peaks of 40.12% Mn^{2+} (640.4 eV), 30.34% Mn^{3+} (642.0 eV), and 29.54% Mn^{4+} (643.8 eV), corresponding to the spin-orbit peaks of Mn with mixed valence states of +2, +3, and +4, respectively [35].

3.2. Electrochemical evaluation

Electrochemical properties of the MnO_x/N-rGO$_{ae}$ SCs were evaluated by CV, GCD, and EIS. Symmetric SCs with four types of electrolytes including 0.5 M Na_2SO_4, 0.5 M Na_2SO_4 with 1 mM $K_4[Fe(CN)_6]$, [BMP][DCA], and [BMP][DCA] with 1 mM $K_4[Fe(CN)_6]$
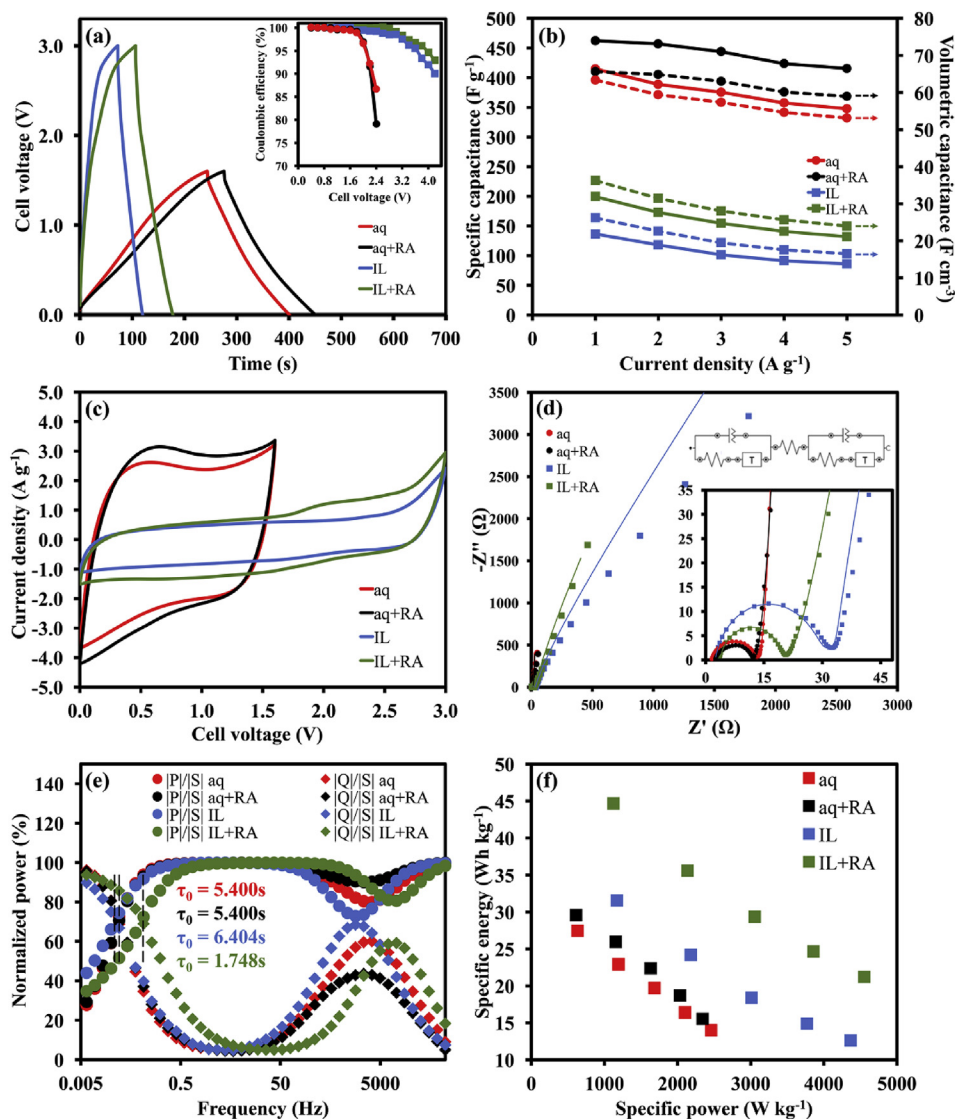

Fig. 4. (a) GCDs of SCs at 1 A g^{-1} with inset coulombic efficiency at 2 A g^{-1} of 0.5 M Na_2SO_4 (aq), 0.5 M Na_2SO_4 with 1 mM $K_4[Fe(CN)_6]$ (aq+RA), [BMP][DCA] (IL), and [BMP][DCA] with 1 mM $K_4[Fe(CN)_6]$ (IL+RA), (b) Specific and volumetric capacitances as a function of applied currents, (c) CVs of SCs at 25 mV s^{-1}, (d) Nyquist plots (experimental and simulation values are shown by point and line, respectively), (e) complex power analysis, and (f) Ragone plot of MnO_x/N-rGO$_{ae}$ with different electrolytes.

were fabricated and tested. Note, Fig. S3a shows the calculated specific capacitances at different scan rates and Fig. S3b shows CV curves (at 25 mV s^{-1}) of the MnO$_x$/N-rGO$_{ae}$ in [BMP][DCA] with different K$_4$[Fe(CN)$_6$] concentrations. It can be observed that both specific capacitance and response current increase when the concentrations of K$_4$[Fe(CN)$_6$] increase and reach the highest value at 1 mM, which is the optimum condition. To determine the voltage stability window of SCs, GCDs (inset of Fig. 4a) were carried out at 2 A g^{-1} with the extending potential window to 2.4 V for aqueous electrolyte and 4.2 V for ionic liquid electrolyte. The aqueous electrolyte-based SCs display an almost 100**%** coulombic efficiency (CE) and then decay after potential window beyond 1.6 V due to the decomposition of electrolyte. On the other hand, beyond 98**%** CE was achieved by using ionic liquid electrolyte with 3.0 V voltage window. Note that the GCD curves of SC using 0.5 M Na$_2$SO$_4$ with 1 mM K$_4$[Fe(CN)$_6$] at 1 A g^{-1} (Fig. 4a) shows slightly lower CE when compared to the SC using 0.5 M Na$_2$SO$_4$ electrolyte due to the ion shuttle effect characteristic, which is a random movement of the redox additive species between two electrodes through the porous separator [13]. In contrast, when K$_4$[Fe(CN)$_6$] was added to **[BMP] [DCA]** electrolyte, it does not only enhance CE but also reduce the internal resistance of the system. This is because K$_4$[Fe(CN)$_6$] can act as additional ions accomplishing the formation of surface redox reaction. The specific capacitance was then calculated from GCD technique as shown in Fig. 4b. The specific capacitance of SCs using 0.5 M Na$_2$SO$_4$ and **[BMP][DCA]** is 414.8 F g^{-1} and 136.5 F g^{-1} at 1 A g^{-1}, respectively. Interestingly, when 1 mM K$_4$[Fe(CN)$_6$] was added to both 0.5 M Na$_2$SO$_4$ and [BMP][DCA], the specific capacitance of SCs significantly increases to 462.4 F g^{-1} and 199.4 F g^{-1} at 1 A g^{-1}, respectively. Note, the volumetric capacitances at 1 A g^{-1} are 63.4, 65.6, 26.2, and 36.3 F cm^{-3} for 0.5 M Na$_2$SO$_4$, 0.5 M Na$_2$SO$_4$ with 1 mM K$_4$[Fe(CN)$_6$], [BMP][DCA], and [BMP][DCA] with 1 mM K$_4$[Fe(CN)$_6$], respectively. In addition, CV results (Fig. 4c and S4)

also show the same tendency to the GCDs, the specific capacitance of SCs increases when 1 mM K$_4$[Fe(CN)$_6$] is introduced to the system. Moreover, the CVs at 25 mV s^{-1} exhibit a distinct increase in the response current as the 1 mM K$_4$[Fe(CN)$_6$] is added to the electrolytes indicating that it can remarkably enhance the electrochemical performance of the MnO$_x$/N-rGO$_{ae}$ SCs. Note, the specific capacitance slightly decreases as the scan rate increases due to the diffusion limit. The CV and GCD profiles at different scan rates and applied currents are also displayed in Fig. S5. The shuttling of K$_4$[Fe(CN)$_6$] species in aqueous electrolyte can also be observed in Nyquist plots (Fig. 4d). The SC using 0.5 M Na$_2$SO$_4$ with 1 mM K$_4$[Fe(CN)$_6$] appears to be slightly deviated from the y-axis at a low-frequency region (as compared to 0.5 M Na$_2$SO$_4$). This phenomenon can be explained by the diffusion-limited chemical leakage current through the separator [13]. However, 1 mM K$_4$[Fe(CN)$_6$] redox additive slightly reduces the charge transfer resistance (R$_{ct}$) from 11.68 Ω to 9.72 Ω due to its high ionic mobility [13]. Moreover, after 1 mM K$_4$[Fe(CN)$_6$] is added to [BMP][DCA], there is a significant decrease in R$_{ct}$ from 28.90 Ω to 17.08 Ω. The specific capacitances of SCs calculated from EIS analysis (Fig. S6a) using 0.5 M Na$_2$SO$_4$ and 0.5 M Na$_2$SO$_4$ with 1 mM K$_4$[Fe(CN)$_6$] are 599.02 F g^{-1} and 617.04 F g^{-1} at an applied frequency of 1 mHz, respectively. Also, the relaxation-time constant (τ_0) of SCs, which is a minimum time required for fully discharging the stored charges, calculated from complex power diagram is shown in Fig. 4e [25]. τ_0 values are 5.400 s for both 0.5 M Na$_2$SO$_4$ and 0.5 M Na$_2$SO$_4$ with 1 mM K$_4$[Fe(CN)$_6$], implying a fast kinetic of redox additive (even at higher capacitance). On the other hand, the τ_0 of the SC using [BMP][DCA] with 1 mM K$_4$[Fe(CN)$_6$] is significantly lower (1.748 s) than that of the pristine [BMP][DCA] (6.404 s) (Fig. 3e), implying the faster discharge process. The reason behind this remarkable improvement on τ_0 and R$_{ct}$ of [BMP][DCA] electrolyte with 1 mM K$_4$[Fe(CN)$_6$] originates via the additional active species and surface
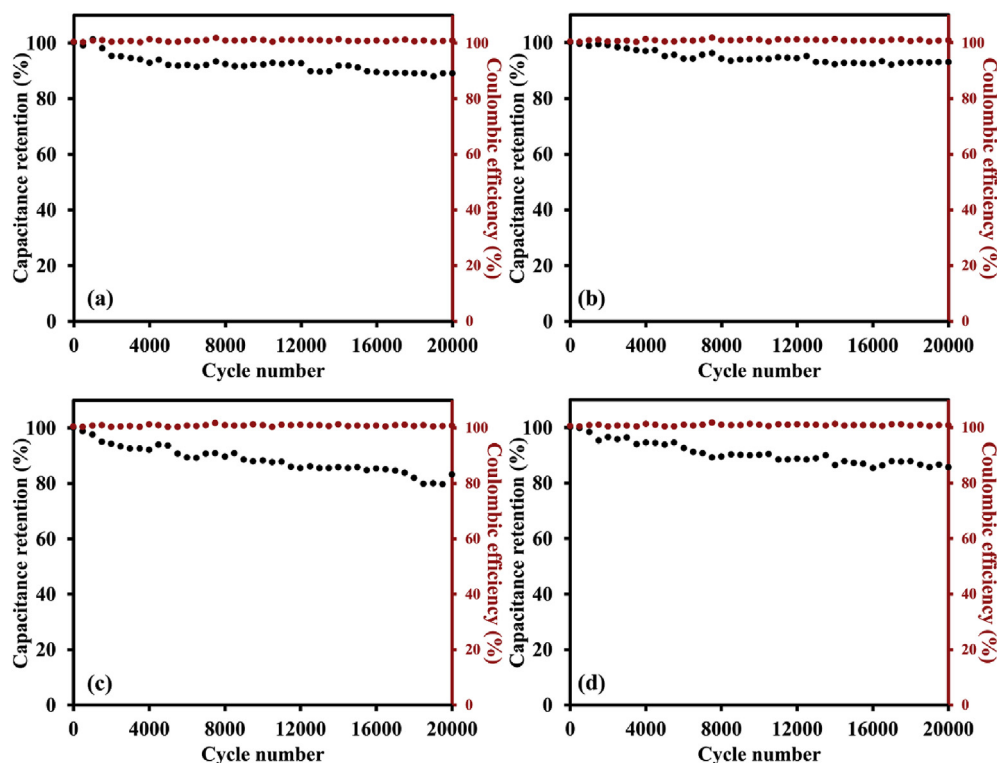

Fig. 5. Capacitance retention and coulombic efficiency of SCs at 3 A g^{-1} over 20,000 cycles using (a) 0.5 M Na$_2$SO$_4$, (b) 0.5 M Na$_2$SO$_4$ with 1 mM K$_4$[Fe(CN)$_6$], (c) [BMP][DCA], and (d) [BMP][DCA] with 1 mM K$_4$[Fe(CN)$_6$].
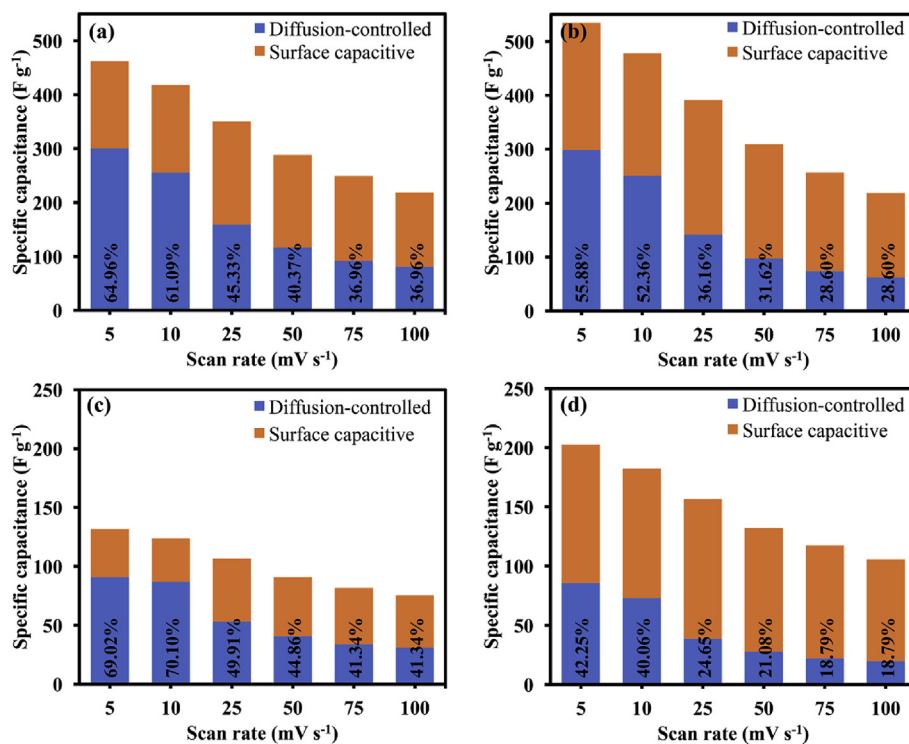
Fig. 6. Calculated cell capacitive contribution (%) and diffusion-controlled capacitance (%) of MnO$_x$/N-rGO$_{ae}$ supercapacitors in (a) 0.5 M Na$_2$SO$_4$, (b) 0.5 M Na$_2$SO$_4$ with 1 mM K$_4$[Fe(CN)$_6$], (c) [BMP][DCA], and (d) [BMP][DCA] with 1 mM K$_4$[Fe(CN)$_6$] at different scan rates. Note, the percentages represent the calculated diffusion-controlled capacitance contribution.

capacitive mechanism (non-diffusion limited). Also, the SC using [BMP][DCA] with 1 mM K$_4$[Fe(CN)$_6$] exhibits higher specific capacitance of 144.45 F g^{-1} compared to 118.14 F g^{-1} for [BMP][DCA] (Fig. S6a). τ_0 calculated from Bode plot at 45° (Fig. S6b) shows the same tendency as the complex power analysis with the τ_0 of 5.663 s, 5.400 s, 6.312 s, and 1.878 s for 0.5 M Na$_2$SO$_4$, 0.5 M Na$_2$SO$_4$ with 1 mM K$_4$[Fe(CN)$_6$], [BMP][DCA], and [BMP][DCA] with 1 mM K$_4$[Fe(CN)$_6$], respectively.

Specific energy and power of the as-fabricated SCs were calculated from GCDs as shown in the Ragone plot (Fig. 4f). The SC using [BMP][DCA] with 1 mM K$_4$[Fe(CN)$_6$] exhibits superior performance on both specific energy (44.68 Wh kg^{-1} at 1121.6 W kg^{-1}) and specific power (4551.4 W kg^{-1} at 21.24 Wh kg^{-1}) when compared to the [BMP][DCA]. This could be explained by the significant difference in the internal resistance, which plays an important role limiting both cell voltage windows and capacitance of the [BMP][DCA]. In aqueous electrolyte systems, K$_4$[Fe(CN)$_6$] is substantial in enhancing the redox activity leading to the higher performance SCs. In addition, the capacity retention of SCs for long-term usage can also be improved by adding a very small amount of redox mediator into the electrolyte as demonstrated in this work using 0.5 M Na$_2$SO$_4$, 0.5 M Na$_2$SO$_4$ with 1 mM K$_4$[Fe(CN)$_6$], [BMP][DCA], and [BMP][DCA] with 1 mM K$_4$[Fe(CN)$_6$]. After charged and discharged over 20,000 cycles, SCs can retain over 87.9%, 92.1%, 79.7%, and 85.3%, respectively with CE close to 100% for all systems (Fig. 5). After 20,000 cycles, the composition of four manganese oxide compounds was also characterized by XRD technique. First, the as-prepared MnO$_x$/N-rGO$_{ae}$ composes of 24.1% MnO$_2$, 29.3% Mn$_2$O$_3$, 33.7% Mn$_3$O$_4$, and 12.9% MnO with an average oxidation state of 3.01. After 20,000 cycles tested in four different electrolytes, the compositions of manganese oxide are changed as shown in Table S1 and Fig. S7. The average oxidation states after tested are 3.01, 3.02, 2.88, and 2.92 for 0.5 M Na$_2$SO$_4$ (aq), 0.5 M Na$_2$SO$_4$ with 1 mM

K$_4$[Fe(CN)$_6$] (aq+RA), [BMP][DCA] (IL), and [BMP][DCA] with 1 mM K$_4$[Fe(CN)$_6$] (IL+RA), respectively. As the results, the changes of manganese oxide compositions could be a major reason leading to the decreasing capacity retention after long cycling.

To clarify the behavior of redox additive in both aqueous and ionic liquid electrolyte, the charge storage contribution of hybrid SCs were analyzed (Fig. 6) [37,38]. The response current on a specific applied scan rate depends on whether the reaction is surface-limited or diffusion-limited. The results show the notable increase in surface capacitive activity for both aqueous and ionic liquid electrolyte system when the scan rates are increased due to an additional reversible faradaic capacitive of K$_4$[Fe(CN)$_6$] redox additive on the active surface of the MnO$_x$/N-rGO$_{ae}$ (reaction 1) [13]. Note that the diffusion-controlled contribution does significantly drop, indicating the underused of the inner active site and the diffusion limit of ions at fast sweep rates [25].

$$[Fe(CN)_6]^{4-} \leftrightarrow [Fe(CN)_6]^{3-} + e^- \tag{1}$$

In order to explain the reaction mechanism, the oxidation state of Mn in the MnO$_x$/N-rGO$_{ae}$ electrode using different electrolytes under certain potentials (charge/discharge) was directly examined by *in situ* Mn K-edge XAS technique with chronoamperometry. Fig. 7a, c, e, and g demonstrate the series of spectra at different applied potentials of the MnO$_x$/N-rGO$_{ae}$ electrode in 0.5 M Na$_2$SO$_4$, 0.5 M Na$_2$SO$_4$ with 1 mM K$_4$[Fe(CN)$_6$], [BMP][DCA], and [BMP][DCA] with 1 mM K$_4$[Fe(CN)$_6$], respectively. All the spectra exhibit an indistinguishable shape, revealing a comparability structural characteristic of manganese under various applied potentials. However, the shift towards a higher energy when the applied potential is increased during the charging process (reflecting an increasing in the oxidation state of Mn ion) and the return to its original state as the potential is decreased (decreasing in the
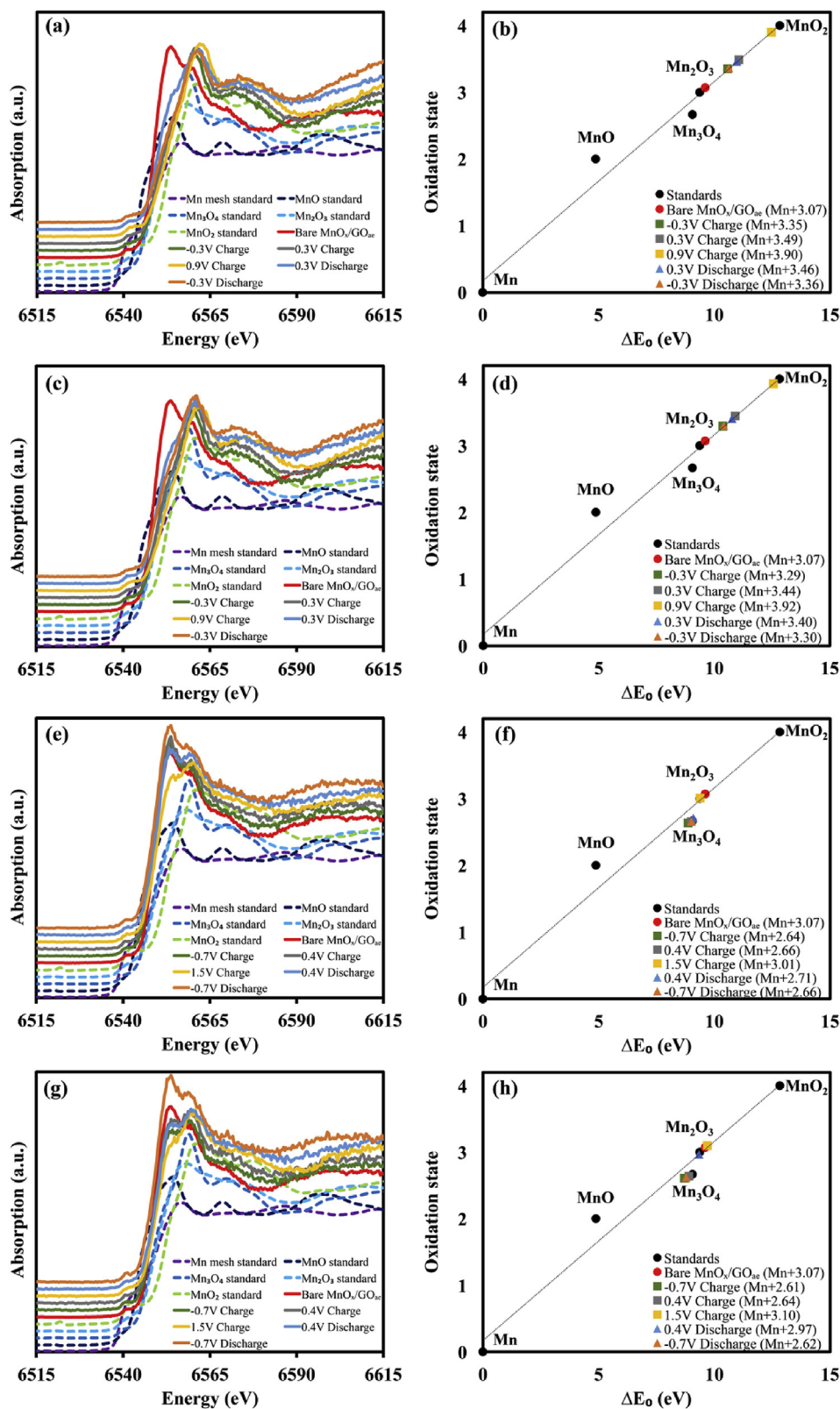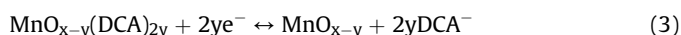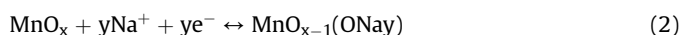
Fig. 7. *In situ* Mn K-edge XANES spectra of the MnO$_x$/GO$_{ae}$ electrode using (a) 0.5 M Na$_2$SO$_4$ (aq), (c) 0.5 M Na$_2$SO$_4$ with 1 mM K$_4$[Fe(CN)$_6$] (aq+RA), (e) [BMP][DCA] (IL), and (g) [BMP][DCA] with 1 mM K$_4$[Fe(CN)$_6$] (IL+RA) as well as the variation of the Mn valence state with respect to the applied potential in (b) aq, (d) aq+RA, (f) IL, and (h) IL+RA electrolyte. Five reference samples with their E$_0$ values are also shown. Note, potential vs. SCE (aq and aq+RA) or Ag/AgCl screen-printed electrode (IL and IL+RA).

Table 1
E_0 and Mn oxidation states of the MnO_x/N-rGO$_{ae}$ electrode using 0.5 M Na$_2$SO$_4$, 0.5 M Na$_2$SO$_4$ with 1 mM K$_4$[Fe(CN)$_6$], [BMP][DCA], and [BMP][DCA] with 1 mM K$_4$[Fe(CN)$_6$] determined from *in situ* Mn K-edge XANES spectra.

Electrolytes	Applied potential (V)	E_0 (eV)	Oxidation state
0.5 M Na$_2$SO$_4$	−0.3 V Charge	6549.82	3.35
	0.3 V Charge	6550.30	3.49
	0.9 V Charge	6551.71	3.90
	0.3 V Discharge	6550.21	3.46
	−0.3 V Discharge	6549.87	3.36
0.5 M Na$_2$SO$_4$ + 1 mM K$_4$[Fe(CN)$_6$]	−0.3 V Charge	6549.62	3.29
	0.3 V Charge	6550.14	3.44
	0.9 V Charge	6551.81	3.92
	0.3 V Discharge	6550.01	3.40
	−0.3 V Discharge	6549.65	3.30
[BMP][DCA]	−0.7 V Charge	6548.11	2.64
	0.4 V Charge	6548.24	2.66
	1.5 V Charge	6548.63	3.01
	0.4 V Discharge	6548.34	2.71
	−0.7 V Discharge	6548.25	2.66
[BMP][DCA] + 1 mM K$_4$[Fe(CN)$_6$]	−0.7 V Charge	6547.95	2.61
	0.4 V Charge	6548.14	2.64
	1.5 V Charge	6548.94	3.10
	0.4 V Discharge	6548.58	2.97
	−0.7 V Discharge	6548.02	2.62

oxidation state of Mn ion) during the discharging process can be observed in all figures (see Table 1) [8,39,40]. Furthermore, the valence states of Mn can be identified by the absorption threshold energy (E_0) obtaining from the first derivative peak (first inflection point on the main edge) [41]. The E_0 values of the MnO_x/N-rGO$_{ae}$ electrode in all electrolytes are illustrated in Fig. 7b, d, f, and h [39]. The valence states of Mn ion in various conditions are also listed in Table 1. The difference in potential range is observed due to the variation of redox reaction mechanism as proposed below for aqueous (reaction 2) and ionic liquid (reaction 3) electrolytes. Interestingly, with the presence of redox additive, *in situ* XAS shows a wider oxidation state variation range implying to the higher redox activity on the electrode surface, originated from the additional redox charge transfer between MnO_x and $Fe(CN)_6^{3-}$/$Fe(CN)_6^{4-}$. These results confirm the faradaic charge transfer interaction between redox additive and MnO_x. Moreover, the XAS result also confirms the reversibility of the redox reaction of MnO_x over the potential range in all electrolytes [8,39]. Note, the oxidation state of Mn in the as-prepared MnO_x/N-rGO$_{ae}$ electrode is +3.07, which slightly differs from the XPS result due to the difference of probing depths between two techniques.

$$MnO_x + yNa^+ + ye^- \leftrightarrow MnO_{x-1}(ONa_y) \quad (2)$$

$$MnO_{x-y}(DCA)_{2y} + 2ye^- \leftrightarrow MnO_{x-y} + 2yDCA^- \quad (3)$$

4. Conclusions

A new composite material between EDLC-type N-rGO$_{ae}$ with an N content of ca. 8 at% and pseudocapacitor-type MnO_x nanoparticles with a diameter of <20 nm was synthesized by the solvothermal process. The MnOx/N-rGO$_{ae}$ was used as the electrode material of hybrid supercapacitors storing charges via both EDLC and surface redox reaction. A new electrolyte of [BMP][DCA]) ionic liquid with a redox additive (K$_4$[Fe(CN)$_6$]) was also employed to further improve the performance of hybrid supercapacitors. The as-fabricated supercapacitor exhibits an excellent specific energy and power of 44.7 Wh kg^{-1} and 4551.4 W kg^{-1}, respectively. *In situ* electrochemical XAS shows that with the presence of redox

additive in the electrolytes a wide oxidation state variation range of Mn in the MnO_x/N-rGO$_{ae}$ composite can be observed indicating high redox activities and confirming the faradaic charge transfer interaction between redox additive and MnO_x. Besides, the *in situ* XAS result also confirms the reversibility of the redox reaction of MnO_x indicating that the hybrid supercapacitor using the ionic liquid electrolyte with a redox additive may be used in high-energy applications.

Appendix A. Supplementary data

Supplementary data related to this article can be found at https://doi.org/10.1016/j.electacta.2018.03.116.

References

[1] Y. Gogotsi, P. Simon, True performance metrics in electrochemical energy storage, Science 334 (2011) 917–918.
[2] P. Simon, Y. Gogotsi, Materials for electrochemical capacitors, Nat. Mater. 7 (2008) 845–854.
[3] D.P. Dubal, O. Ayyad, V. Ruiz, P. Gomez-Romero, Hybrid energy storage: the merging of battery and supercapacitor chemistries, Chem. Soc. Rev. 44 (2015) 1777–1790.
[4] M.F. El-Kady, V. Strong, S. Dubin, R.B. Kaner, Laser scribing of high-performance and flexible graphene-based electrochemical capacitors, Science 335 (2012) 1326–1330.
[5] J.M. Tarascon, M. Armand, Issues and challenges facing rechargeable lithium batteries, Nature 414 (2001) 359–367.
[6] Y. Huang, Y. Li, Z. Hu, G. Wei, J. Guo, J. Liu, A carbon modified MnO$_2$ nanosheet array as a stable high-capacitance supercapacitor electrode, J. Mater. Chem. A 1 (2013) 9809–9813.
[7] W. Wei, X. Cui, W. Chen, D.G. Ivey, Manganese oxide-based materials as electrochemical supercapacitor electrodes, Chem. Soc. Rev. 40 (2011) 1697–1721.
[8] M. Toupin, T. Brousse, D. Bélanger, Charge storage mechanism of MnO$_2$ electrode used in aqueous electrochemical capacitor, Chem. Mater. 16 (2004) 3184–3190.
[9] Y. Song, T.Y. Liu, B. Yao, M.Y. Li, T.Y. Kou, Z.H. Huang, D.Y. Feng, F.X. Wang, Y.X. Tong, X.X. Liu, Y. Li, Ostwald ripening improves rate capability of high mass loading manganese oxide for supercapacitors, Acs Energy Lett. 2 (2017) 1752–1759.
[10] J. Shin, D. Shin, H. Hwang, T. Yeo, S. Park, W. Choi, One-step transformation of MnO2 into MnO2-x@carbon nanostructures for high performance supercapacitors using structure guided combustion waves, J. Mater. Chem. A 5 (2017) 13488–13498.
[11] N. Phattharasupakun, J. Wutthiprom, P. Chiochan, P. Suktha, M. Suksomboon, S. Kalasina, M. Sawangphruk, Turning conductive carbon nanospheres into nanosheets for high-performance supercapacitors of MnO2 nanorods, Chem. Commun. 52 (2016) 2585–2588.
[12] M.-K. Song, S. Cheng, H. Chen, W. Qin, K.-W. Nam, S. Xu, X.-Q. Yang, A. Bongiorno, J. Lee, J. Bai, T.A. Tyson, J. Cho, M. Liu, Anomalous pseudocapacitive behavior of a nanostructured, mixed-valent manganese oxide film for electrical energy storage, Nano Lett. 12 (2012) 3483–3490.
[13] J. Lee, S. Choudhury, D. Weingarth, D. Kim, V. Presser, High performance hybrid energy storage with potassium ferricyanide redox electrolyte, ACS Appl. Mater. Interfaces 8 (2016) 23676–23687.
[14] S. Roldán, M. Granda, R. Menéndez, R. Santamaría, C. Blanco, Mechanisms of energy storage in carbon-based supercapacitors modified with a quinoid redox-active electrolyte, J. Phys. Chem. C 115 (2011) 17606–17611.
[15] S.T. Senthilkumar, R.K. Selvan, Y.S. Lee, J.S. Melo, Electric double layer capacitor and its improved specific capacitance using redox additive electrolyte, J. Mater. Chem. A 1 (2013) 1086–1095.
[16] G.K. Veerasubramani, K. Krishnamoorthy, S.J. Kim, Improved electrochemical performances of binder-free CoMoO$_4$ nanoplate arrays@Ni foam electrode using redox additive electrolyte, J. Power Sources 306 (2016) 378–386.
[17] K. Chen, F. Liu, D. Xue, S. Komarneni, Carbon with ultrahigh capacitance when graphene paper meets K$_3$Fe(CN)$_6$, Nanoscale 7 (2015) 432–439.
[18] S.T. Senthilkumar, R.K. Selvan, J.S. Melo, Redox additive/active electrolytes: a

novel approach to enhance the performance of supercapacitors, J. Mater. Chem. A 1 (2013) 12386–12394.

[19] S. Yamazaki, T. Ito, M. Yamagata, M. Ishikawa, Non-aqueous electrochemical capacitor utilizing electrolytic redox reactions of bromide species in ionic liquid, Electrochim. Acta 86 (2012) 294–297.

[20] S. Sathyamoorthi, V. Suryanarayanan, D. Velayutham, Organo-redox shuttle promoted protic ionic liquid electrolyte for supercapacitor, J. Power Sources 274 (2015) 1135–1139.

[21] T.Y. Kim, H.W. Lee, M. Stoller, D.R. Dreyer, C.W. Bielawski, R.S. Ruoff, K.S. Suh, High-performance supercapacitors based on poly(ionic liquid)-modified graphene electrodes, ACS Nano 5 (2011) 436–442.

[22] P.-L. Huang, X.-F. Luo, Y.-Y. Peng, N.-W. Pu, M.-D. Ger, C.-H. Yang, T.-Y. Wu, J.-K. Chang, Ionic liquid electrolytes with various constituent ions for graphene-based supercapacitors, Electrochim. Acta 161 (2015) 371–377.

[23] M. Sawangphruk, J. Limtrakul, Effects of pore diameters on the pseudocapacitive property of three-dimensionally ordered macroporous manganese oxide electrodes, Mater. Lett. 68 (2012) 230–233.

[24] M. Sawangphruk, P. Srimuk, P. Chiochan, A. Krittayavathananon, S. Luanwuthi, J. Limtrakul, High-performance supercapacitor of manganese oxide/reduced graphene oxide nanocomposite coated on flexible carbon fiber paper, Carbon 60 (2013) 109–116.

[25] T. Pettong, P. Iamprasertkun, A. Krittayavathananon, P. Sukha, P. Sirisinudomkit, A. Seubsai, M. Chareonpanich, P. Kongkachuichay, J. Limtrakul, M. Sawangphruk, High-performance asymmetric supercapacitors of MnCo$_2$O$_4$ nanofibers and N-Doped reduced graphene oxide aerogel, ACS Appl. Mater. Interfaces 8 (2016) 34045–34053.

[26] H. Yin, C. Song, Y. Wang, S. Li, M. Zeng, Z. Zhang, Z. Zhu, K. Yu, Influence of morphologies and pseudocapacitive contributions for charge storage in V$_2$O$_5$ micro/nano-structures, Electrochim. Acta 111 (2013) 762–770.

[27] M. Wu, N.R. Brooks, S. Schaltin, K. Binnemans, J. Fransaer, Electrodeposition of germanium from the ionic liquid 1-butyl-1-methylpyrrolidinium dicyanamide, Phys. Chem. Chem. Phys. 15 (2013) 4955–4964.

[28] J.P. Hallett, T. Welton, Room-temperature ionic liquids: solvents for synthesis and catalysis. 2, Chem. Rev. 111 (2011) 3508–3576.

[29] Y.-T. Hsieh, Y.-C. Chen, I.W. Sun, Electrodeposition of stoichiometric indium antimonide from room-temperature ionic liquid 1-butyl-1-methyl-pyrrolidinium dicyanamide, ChemElectroChem 3 (2016) 638–643.

[30] P. Iamprasertkun, A. Krittayavathananon, A. Seubsai, N. Chanlek, P. Kidkhunthod, W. Sangthong, S. Maensiri, R. Yimnirun, S. Nilmoung, P. Pannopard, S. Ittisanronnachai, K. Kongpatpanich, J. Limtrakul,

M. Sawangphruk, Charge storage mechanisms of manganese oxide nanosheets and N-doped reduced graphene oxide aerogel for high-performance asymmetric supercapacitors, Sci. Rep. 6 (2016) 37560.

[31] P. Iamprasertkun, C. Tanggarnjanavalukul, A. Krittayavathananon, J. Khuntilo, N. Chanlek, P. Kidkhunthod, M. Sawangphruk, Insight into charge storage mechanisms of layered MnO$_2$ nanosheets for supercapacitor electrodes: in situ electrochemical X-ray absorption spectroscopy, Electrochim. Acta 249 (2017) 26–32.

[32] A. Krittayavathananon, T. Pettong, P. Kidkhunthod, M. Sawangphruk, Insight into the charge storage mechanism and capacity retention fading of MnCo$_2$O$_4$ used as supercapacitor electrodes, Electrochim. Acta 258 (2017) 1008–1015.

[33] M. Kim, Y. Hwang, J. Kim, Graphene/MnO$_2$-based composites reduced via different chemical agents for supercapacitors, J. Power Sources 239 (2013) 225–233.

[34] T. Gao, M. Glerup, F. Krumeich, R. Nesper, H. Fjellvåg, P. Norby, Microstructures and spectroscopic properties of cryptomelane-type manganese dioxide nanofibers, J. Phys. Chem. C 112 (2008) 13134–13140.

[35] Y. Wang, W. Lai, N. Wang, Z. Jiang, X. Wang, P. Zou, Z. Lin, H.J. Fan, F. Kang, C.-P. Wong, C. Yang, A reduced graphene oxide/mixed-valence manganese oxide composite electrode for tailorable and surface mountable supercapacitors with high capacitance and super-long life, Energy Environ. Sci. 10 (2017) 941–949.

[36] S. Stankovich, D.A. Dikin, R.D. Piner, K.A. Kohlhaas, A. Kleinhammes, Y. Jia, Y. Wu, S.T. Nguyen, R.S. Ruoff, Synthesis of graphene-based nanosheets via chemical reduction of exfoliated graphite oxide, Carbon 45 (2007) 1558–1565.

[37] S. Ardizzone, G. Fregonara, S. Trasatti, "Inner" and "outer" active surface of RuO$_2$ electrodes, Electrochim. Acta 35 (1990) 263–267.

[38] V. Augustyn, P. Simon, B. Dunn, Pseudocapacitive oxide materials for high-rate electrochemical energy storage, Energy Environ. Sci. 7 (2014) 1597–1614.

[39] J.-K. Chang, M.-T. Lee, W.-T. Tsai, M.-J. Deng, I.W. Sun, X-ray photoelectron spectroscopy and in situ x-ray absorption spectroscopy studies on reversible insertion/desertion of dicyanamide anions into/from manganese oxide in ionic liquid, Chem. Mater. 21 (2009) 2688–2695.

[40] L.-H. Su, X.-G. Zhang, C.-H. Mi, B. Gao, Y. Liu, Improvement of the capacitive performances for Co-Al layered double hydroxide by adding hexacyanoferrate into the electrolyte, Phys. Chem. Chem. Phys. 11 (2009) 2195–2202.

[41] M. Belli, A. Scafati, A. Bianconi, S. Mobilio, L. Palladino, A. Reale, E. Burattini, X-ray absorption near edge structures (XANES) in simple and complex Mn compounds, Solid State Commun. 35 (1980) 355–361.